

Unexpected crystallographic structure, phase transformation, and hardening behavior in the AlCoCrFeNiTi_{0.2} high-entropy alloy after high-dose nitrogen ion implantation

Piotr Jencyk^a, Dariusz M. Jarzabek^{a,*}, Zhang Lu^b, Elżbieta Gadalińska^c, Neonila Levintant-Zayonts^a, Yong Zhang^b

^a Institute of Fundamental Technological Research, Polish Academy of Sciences, Pawińskiego 5B, 02-106 Warsaw, Poland

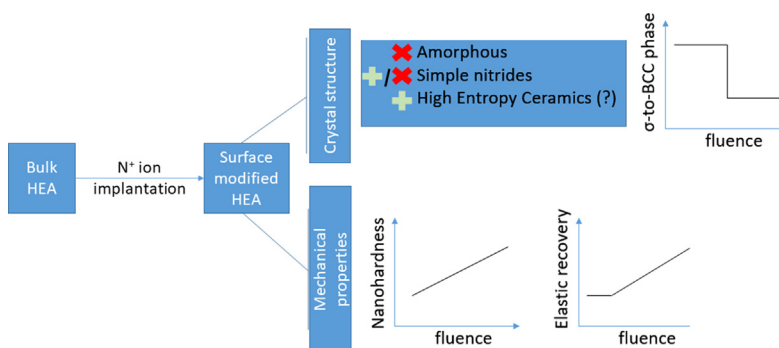
^b Beijing Advanced Innovation Center of Materials Genome Engineering, State Key Laboratory for Advanced Metals and Materials, University of Science and Technology Beijing, 30 Xueyuan Road, Beijing 100083, China

^c Łukasiewicz Research Network – Institute of Aviation, Materials and Structures Research Center, Al. Krakowska 110/114, 02-256 Warsaw, Poland

HIGHLIGHTS

- Very high dose of nitrogen ions implanted into AlCoCrFeNiTi_{0.2} high entropy alloy.
- Unidentified XRD spectrum which we tentatively attribute to the creation of new high or medium entropy ceramics.
- Promising and interesting properties – higher hardness and wear resistance on one hand and higher hardness-to-Young's modulus ratio on the other hand.

GRAPHICAL ABSTRACT



ARTICLE INFO

Article history:

Received 24 January 2022

Revised 10 March 2022

Accepted 16 March 2022

Available online 23 March 2022

Keywords:

High-entropy alloys
High-entropy ceramics
Ion implantation
Irradiation
Phase transformation

ABSTRACT

Harsh environments, such as nuclear power plants, require the development of materials with stable properties when exposed to radiation/bombardment conditions. In this work, a bulk high-entropy alloy (HEA) was implanted with nitrogen ions accelerated at 50 kV to induce and study crystal structural defects. X-ray powder diffraction (XRD) showed that the studied HEA consisted of two phases— σ and body-centered cubic (BCC)—and underwent the σ to BCC phase transformation due to ion bombardment. Unexpectedly, XRD peaks of implanted samples could not be assigned to any known simple nitride, a finding that suggests the creation of new high- or medium-entropy ceramics. Studies of the mechanical and tribological properties with the use of nanoindentation and scratch tests revealed a hardening of both phases of the implanted surface and higher wear resistance. There were also surprising increases in the hardness-to-Young's modulus ratio and elastic recovery for both phases. The results are promising not only for the nuclear applications, but also for space applications, mechanical engineering, and tribology.

© 2022 The Author(s). Published by Elsevier Ltd. This is an open access article under the CC BY-NC-ND license (<http://creativecommons.org/licenses/by-nc-nd/4.0/>).

1. Introduction

High-entropy alloys (HEAs), a new alloy system that was discovered in 2004 by Yeh et al. [1], have provided a new approach to alloy design. The main idea of such systems is to use five (or

* Corresponding author.

E-mail address: djarz@ippt.pan.pl (D.M. Jarzabek).

more) alloying elements in equimolar (or near equimolar) fractions as well to provide a random distribution of atoms in lattice sites of a crystal structure. These innovative materials have generated considerable research interest. However, it is worth recalling what Tsai and Yeh [2] stated: in addition to simple solid solution phases, intermediate phases in such materials are of great interest and should not be omitted. Furthermore, there has been a recent separation into HEAs with a single-phase microstructure, as was expected by the first developers, and those with more than one phase. The second group can be named compositionally complex alloys (CCAs) [3]. Broad scientific interest in CCAs originates from the expectation of their superior mechanical and physical properties, which have been confirmed experimentally [4]. Compared with conventional alloys, many HEAs, especially CCAs, have considerably better strength-to-weight ratios; enhanced tensile strength; and improved fracture, corrosion, and oxidation resistance [5–8]. However, it would be difficult to use them commercially in most structural engineering applications, where much cheaper, yet still suitable materials—such as steels or aluminum (Al) or magnesium (Mg) alloys—are currently used. Hence, one should pursue applications in which HEAs are still attractive, that is, applications in which all other materials fail to function properly. For example, interactions with irradiation or high-energy particles usually induce severe and challenging structural changes of conventional materials. This topic is of particular importance for future nuclear and fusion power plants [6] and space applications [9].

Ion implantation is a technique that can significantly change the physical, mechanical, tribological, or electrical properties of a solid by bombarding the surface with high-energy ions [10]. It can also be used to imitate the effects of neutron radiation [11]. The incident ions alter the elemental distribution of the bombarded material while stopping in the surface layer (usually penetrating hundreds of nanometers) and causing many chemical and physical changes. The incident ion energy is transferred to the electrons and atomic nuclei of the bombarded material, which, in turn, causes a structural change—the crystal structure of the material can be transformed or totally destroyed by the energetic collision cascades. Hence, this technique, which is broadly used in materials science and engineering, could be applied to study the structural changes of HEAs induced by irradiation or high-energy ions. It should be noted that the materials that have the highest resistance to such changes have a body-centered cubic (BCC) structure. This property of BCC metals and alloys is mainly due to their enhanced resistance to void swelling, lower primary defect production, and better defect evolution behavior [12–14]. Furthermore, HEAs are probably more resistant to irradiation damage than conventional alloys. Unfortunately, there is not much research on the irradiation resistance of CCAs. Due to their complex nature and the metastability of their constituents, irradiation-induced phase transformations may occur more often than in single-phase HEAs. However, radiation-enhanced diffusion, which results in phase separation and transformation, has been observed for many conventional alloys and intermetallics [15]. For example, Nastasi and Mayer [16] showed that upon xenon (Xe) or neon (Ne) ion implantation, Ni_2Al_3 transforms into an ordered cubic phase of NiAl . Furthermore, Gandy et al. [17] reported radiation-induced sigma (σ) to BCC phase transformation in SiFeVCr . This result is very interesting due to the fact that the σ phase is very hard but brittle, so it may substantially influence the overall mechanical properties of the material [18]. Hence, controlling the amount of this phase is crucial for the design of new materials, especially CCAs.

In this paper, we use ion implantation and nanoindentation to study the phase stability of AlCoCrFeNiTiO.2 , an alloy in which the σ phase is dominant. We applied high-fluence nitrogen ion implantation and observed not only the σ to BCC phase transfor-

mation, but also a hardening of both phases. Furthermore, X-ray powder diffraction (XRD) results of the implanted samples revealed an unexpected crystallographic structure that could not be assigned to any simple nitride. We have tentatively attributed these changes to the creation of new high- or medium-entropy ceramics, with interesting and promising properties. The ion-irradiated surface exhibited enhanced ductility and increased wear resistance, both of which are very beneficial for applications in mechanical engineering and tribology.

2. Experimental

2.1. Sample preparation

In this experiment, high-purity Al, cobalt (Co), chromium (Cr), iron (Fe), nickel (Ni), and titanium (Ti) were selected (≥ 99.95 wt % purity for each element). These materials were melted and combined in a ZG-2XF vacuum magnetic levitation induction melting furnace to obtain a large-sized AlCoCrFeNiTiO.2 alloy ingot (about $\Phi 100 \times 120$ mm, with a weight of about 3 kg). The furnace was first evacuated to a vacuum state to remove impurity gases of the materials and then backfilled with high-purity argon gas as a protective atmosphere. During smelting, the electromagnetic force formed by the coil counteracted the gravity of the materials, so the melted materials presented a suspended or quasi-suspended state, which separated the alloy from the inner wall of the crucible, thereby reducing pollution from the crucible. This approach generates high-quality ingots.

2.2. Ion implantation

First, all samples were polished on a Presi Mecatech 334 machine with SiC emery papers (with grit sizes of 320–1200) rotated at 300 rpm. Next, a 3-step final polishing was conducted with a polishing cloth, lubricant, and diamond suspensions of particles 9/3/1 μm and a rotation speed of 200 rpm. After each step, the substrate was rinsed thoroughly with deionized water and isopropanol. A surface roughness (R_a) of ~ 2 nm was achieved, measured by using a stylus profilometer (T8000 Nanoscan). Nitrogen ion implantation was performed by using a typical semi-industrial IMJON implanter, without mass separation, with energy of 50 keV and fluences (dose of nitrogen implanted ions) of 5×10^{16} ions/ cm^2 (D1), 1×10^{17} ions/ cm^2 (D2), and 5×10^{17} ions/ cm^2 (D3). The vacuum level oscillated around 5.6×10^{-5} hPa, the ion beam current was 0.52 mA, and calculation of the doses used was related to an irradiation field of 13 mm^2 . The sample was N^+ ion implanted in frontal geometry. The evolution of the sample temperatures as a function of irradiation time was as follows: the temperature of the samples started from room temperature, then monotonically increased to ~ 177 °C for the D3 dose and ~ 210 °C for the D1 and D2 doses at the end of the irradiation process. These small differences in temperature should not affect the samples microstructure. The measure displacements per atom (dpa) as a function of depth was determined by using the Stopping and Range of Ions in Matter (SRIM) code. The formula to calculate dpa in ion implantation is [19]:

$$\text{dpa} = \frac{\Phi \left(\frac{\text{ions}}{\text{cm}^2} \right) \cdot \gamma}{N}, \quad (1)$$

where Φ is the implantation fluence, γ is the number of displacements produced by a primary knock-on atom (PKA), which can be found in the SRIM output file (VACANCY.TXT, Vacancies by recoils), and N is the atomic density of the implanted material. The density was measured by using Archimedes method.

2.3. Microstructural examination

The surface morphology of the samples was determined by using scanning electron microscopy (SEM), specifically a Zeiss Crossbeam 350 microscope equipped with energy dispersive X-ray spectroscopy (EDS) and electron backscatter diffraction (EBSD) detectors. EDS and EBSD data were analyzed by using the EDAX TEAM software. Next, the crystalline structures of the bulk specimen and the specimens subjected to nitriding were identified by using the Empyrean PANalytical diffractometer with the Rietveld analysis performed with the HighScore software [20]. For the bulk specimen, the diffraction experiment was performed with standard Bragg–Brentano geometry [21], while for the specimens subjected to ion implantation, grazing incidence geometry [22,23] was applied to ensure a constant penetration depth of the incident X-ray beam. All measurements were realized with Cu–K α_1 radiation with a wavelength of $\lambda = 1.540598 \text{ \AA}$. For measurements, capillary optics were used; this approach ensured a quasi-parallel incident beam was used. The diffraction data were acquired with a Pixcel1D-Medipix3 detector. The 2Θ values detected during the experiment were $20\text{--}145^\circ$, with a step size of 0.026° ; the measurement for one step lasted 120 s. The portions of diffractograms without peaks are omitted; therefore, only $30\text{--}90^\circ$ is presented for each sample. The measurement time for the specimens subjected to ion implantation was much longer (15300 s) than the measurement time for the bulk specimen. Moreover, the incident angle for the specimens subjected to ion implantation was constant (2.1°). Providing such a low angle of incidence of the X-ray beam with respect to the surface of the implanted samples made it possible to carry out measurements from a small surface sample volume. This approach was chosen because, based on microscopic measurements, the effect of the implanted process was expected to only affect a small depth.

For the bulk specimen, the general assumption used to calculate the penetration depth was the law of linear mass absorption. The calculation was performed with the built-in algorithm in the HighScore software of the PANalytical apparatus. The algorithm requires the mass absorption coefficient and the expected sample density, which is expressed as a combination of the specific gravity of the material and the estimated packing density. The path length L , which is the length the X-ray travels through a material with given characteristics until 99% of the intensity is absorbed, is calculated first [21]:

$$I_L = I_0 e^{-(\mu/\rho)\rho L} \quad (2)$$

Where I_L is the intensity of the diffracted beam after the path L , I_0 is the intensity of the incident X-ray beam, and μ/ρ is the mass absorption coefficient. Using data calculated with above equation, the penetration depth τ can be established with [21]:

$$\tau = 0.5L \sin\theta \quad (3)$$

The penetration depth for the bulk specimen examined with symmetrical Bragg–Brentano geometry was from $3.429 \text{ }\mu\text{m}$ for $2\theta = 20^\circ$ to $39.498 \text{ }\mu\text{m}$ for $2\theta = 145^\circ$.

The above-presented methodology represents a simplified approach that is only applicable for symmetric cases like Bragg–Brentano geometry for phases analyzed with the grazing incidence methodology. Thus, a different approach to approximate the penetration depth should be applied. The grazing incidence methodology operates in the range of the incident beam angle close to the values of total external reflection. In this case, the formula to determine the penetration depths takes the form [23]:

$$\tau(\alpha) = \frac{\lambda}{4\pi \left[\frac{(\sin^2 \alpha - \sin^2 \alpha_{cr})^2 + 4\beta^2 + \sin^2 \alpha_{cr} - \sin^2 \alpha}{2} \right]} \quad (4)$$

where: α is the angle between the specimen surface and the incident beam, λ is the X radiation wavelength, $\beta = \frac{\mu}{4\pi}$, and μ is the linear absorption of the material. The penetration depth for the experiment performed with the grazing incidence geometry was about $0.7 \text{ }\mu\text{m}$.

2.4. Nanomechanical investigation

Nano-indentation of irradiated films was measured by using *in situ* SEM with the Alemnis nanoindenter equipped with a diamond Berkovich tip. Before measurement, it was calibrated with a reference-fused silica sample. Multi-cycle indentation was applied to obtain the depth profiles of the hardness changes and to compare them with the bulk (non-implanted) specimen. Ten cycles from 3 to 30 mN, with 3 mN steps, were performed. Furthermore, to investigate the differences between the two phases present in the material, small single imprints were made with a maximum load of 3 mN. In this case, the indenter tip was positioned precisely above the area of interest by using the view obtained from SEM. The effect of tip compression and any equipment drift was corrected by the software supplied by the manufacturer. Data gathered after the correction were analyzed with the software supplied by the manufacturer of the device. Hardness, Young's modulus, and indentation depth were calculated with the Oliver–Pharr method, using the same software. From the unloading part of the curve, the top (maximum) 5% and bottom (minimum) 30% were ignored for model fitting.

Scratch tests were performed with the same Alemnis nanoindenter equipped with a diamond spheroconical tip $20 \text{ }\mu\text{m}$ in diameter and with an angle of 60° . The topography of imprints and scratches was investigated by using atomic force microscopy (AFM), with a microscope from Nanosurf (Switzerland). Markers made with a focused ion beam were used to find the structures easily.

3. Results

Based on SEM, EDS (Figs. 1 and 2a), and XRD (Fig. 2b) analyses, the bulk (non-implanted) specimen comprises two phases. The Rietveld analysis revealed that they are the BCC phase and the σ phase with a tetragonal structure (with space group P 42/m n m). The exact elemental compositions of both phases determined by EDS are shown in Table 1, and the corresponding spectra are shown in Fig. 1a and b.

To study the effect of interaction with a beam of high-energy particles, the samples were bombarded with nitrogen ions with energy of 50 keV and fluences (dose of nitrogen implanted ions) of $5 \times 10^{16} \text{ ions/cm}^2$ (D1), $1 \times 10^{17} \text{ ions/cm}^2$ (D2), and $5 \times 10^{17} \text{ ions/cm}^2$ (D3). Fig. 1d shows the concentration of nitrogen ions. Intriguingly, the measured concentration for the D1 and D2 samples are almost the same. We tentatively attributed this result to the high measurement error obtained for both samples. This error is mainly caused by the presence of titanium, which has a peak very close to nitrogen. Nevertheless, the exact values are not essential for this study. Fig. 2a provides a comparison of the nitrogen and chromium EDS signals of the same spot on the D3 sample. Nitrogen is distributed evenly, whereas the difference in chromium distribution indicates the presence of two different phases. The D1 and D2 samples have the same even distribution of nitrogen. It should be noted that after nitrogen ion implantation, both the BCC and σ phases are still present in the samples, but their ratio has been significantly altered. To analyze the samples, two different crystallographic databases were used: ICDD-4 + and Crystallography Open Database (COD). The exact results are presented in Supple-

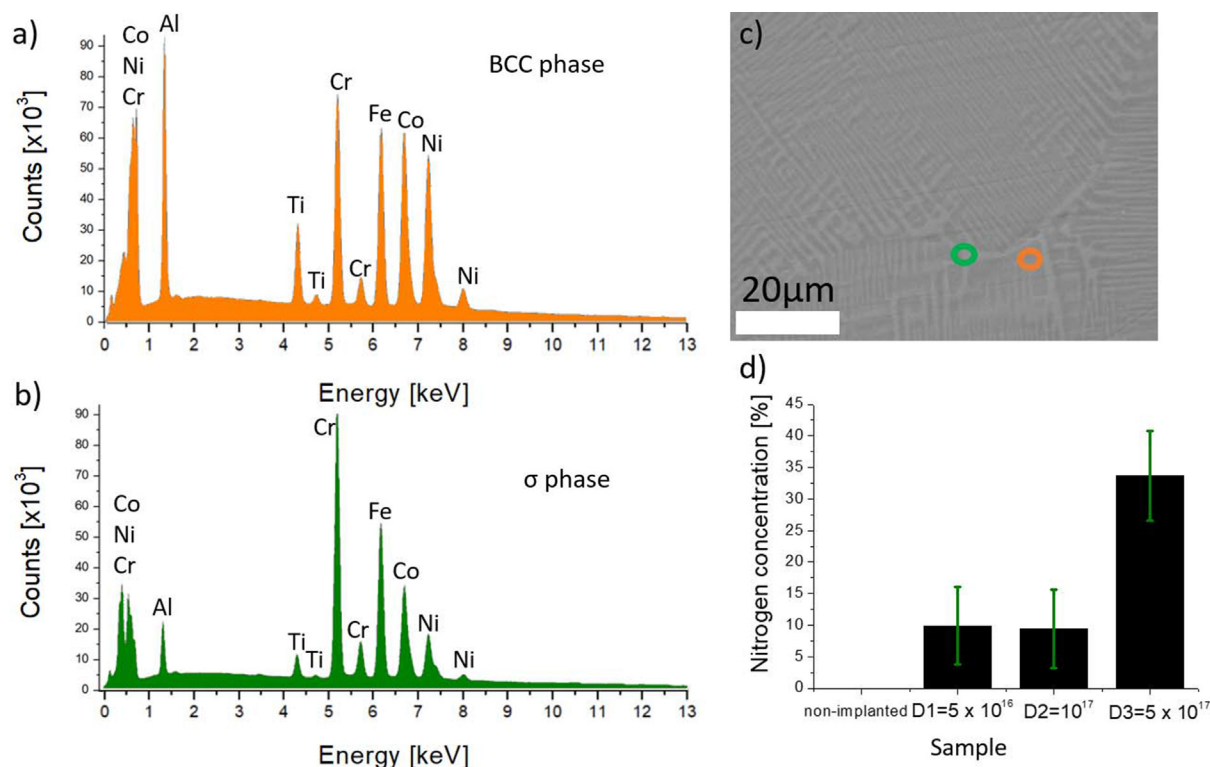


Fig. 1. (a–c) EDS spectra of non-implanted samples based on SEM images of corresponding spots marked with the orange circle for the BCC phase and the green circle for σ phase. (d) The nitrogen concentration for each sample determined with EDS. (For interpretation of the references to colour in this figure legend, the reader is referred to the web version of this article.)

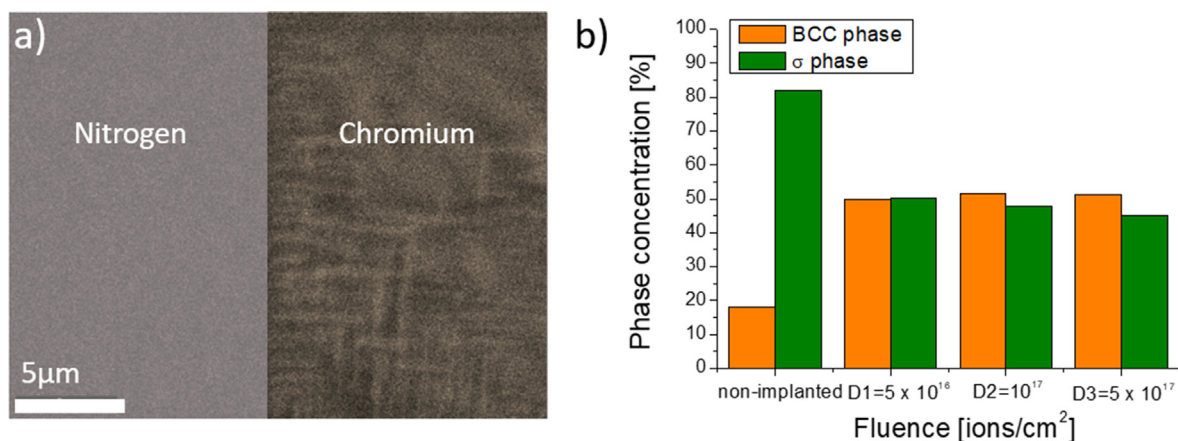


Fig. 2. (a) Representative nitrogen and chromium EDS signals of the same spot. (b) Phase concentrations for each sample calculated by using XRD.

Table 1
Elemental composition of both phases present in bulk (non-implanted) specimen.

BCC phase	Al	Ti	Cr	Fe	Co	Ni
Element						
%at	22.9	4.3	14.7	17.2	20	20.9
Error [%]	7.6	2.6	2.4	2.3	2	2.2
σ phase	Al	Ti	Cr	Fe	Co	Ni
Element						
%at	5.6	1.3	34.3	28.5	19.1	11.3
Error [%]	8.1	3.4	2	2.3	2.2	2.7

mentary Information (Table 1). While the results are consistent for both databases, the exact values differ by single percentages. The differences are larger only in the case of the bulk specimen. The

subsequent analysis is based on ICDD-4 + because it is a larger database and thus small amounts of simple nitrides could be identified.

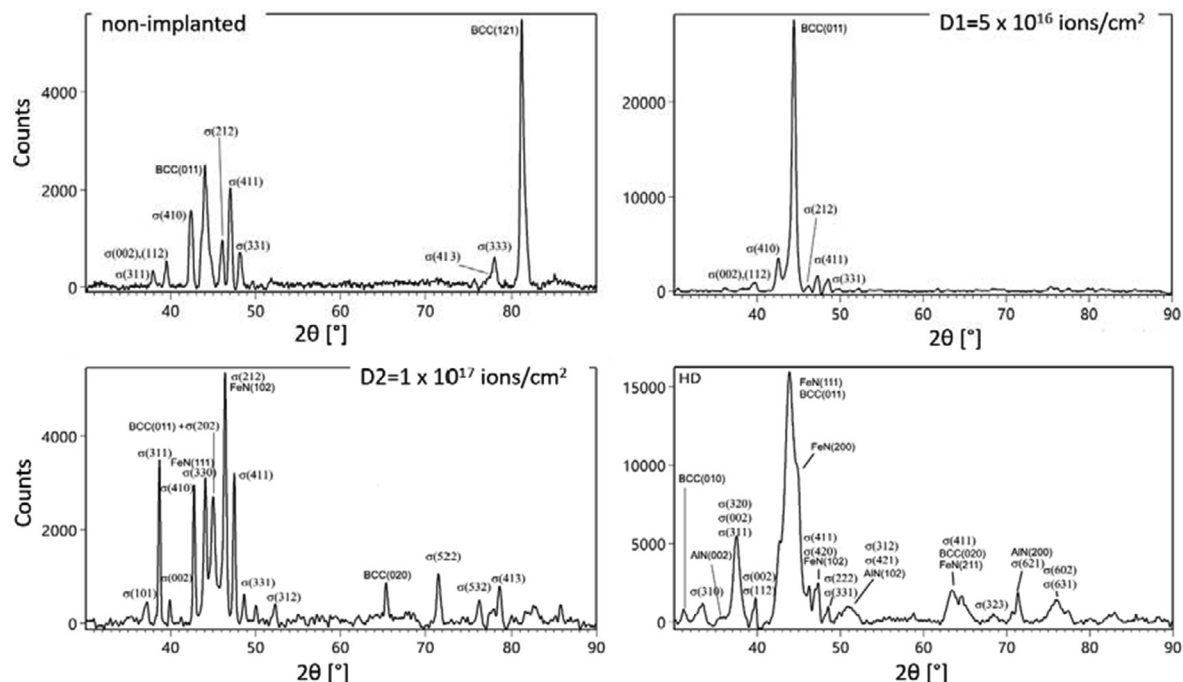


Fig. 3. X-Ray diffractograms for each sample.

The percentage of the BCC phase for the bulk specimen is about 18%; the σ phase comprises the rest of the specimen. Ion implantation led to a rearrangement in the alloy structure: the BCC and σ phases each represent approximately 50% of the specimen (Fig. 2b). Small amounts of hexagonal forms of iron nitride and aluminum nitride also appeared: 0.1%, 0.3%, and 3.5% for the D1, D2, and D3 samples, respectively. The X-ray diffractograms of all four samples are shown in Fig. 3.

To confirm the XRD results, SEM-EBSD characterization was performed (Fig. 4). SEM images indicated that in all the samples there are two different areas, namely lighter and darker (Fig. 4a). EBSD identified them as the BCC and σ phases, a finding that corresponds to the XRD results (Fig. 4b). There are no nitrides, probably due to their negligible volume. The corresponding Kikuchi patterns are shown in Fig. 4b. Furthermore, with confirmed correspondence of the EBSD map to SEM micrographs, much larger areas ($100 \times 100 \mu\text{m}$) were imaged with SEM and the light to dark pixel ratio was determined (Supporting Information, Fig. 1). This

ratio corresponds to the σ to BCC phase ratio. The difference between XRD (ICDD-4 + database) and SEM results is in the range of the measurement error.

SRIM calculations provided additional insight into the ion implantation of the BCC and σ phases (Fig. 5). The ion range for the BCC phase is 64.2 nm and is slightly higher than for the σ phase (59.2 nm). The maximum dpa occurs at 43.5 nm for the BCC phase and 37.5 nm for the σ phase. There are differences in the maximum dpa depending on the fluence. For the D3 sample, the maximum dpa is 222 for the BCC phase and 245 for the σ phase. For the D1 and D2 samples, the maximum dpa is proportionally lower.

Multi-cycle indentation revealed significant changes in the hardness with the depth. Fig. 6a shows an example force–distance curve for each sample. The hardening effect of ion implantation is clearly visible. Furthermore, Fig. 6b presents the results of hardness determination versus indentation depth. For the bulk specimen, there is a visible indentation size effect. On the other hand, the D1 and D2 samples exhibit significantly different behavior:

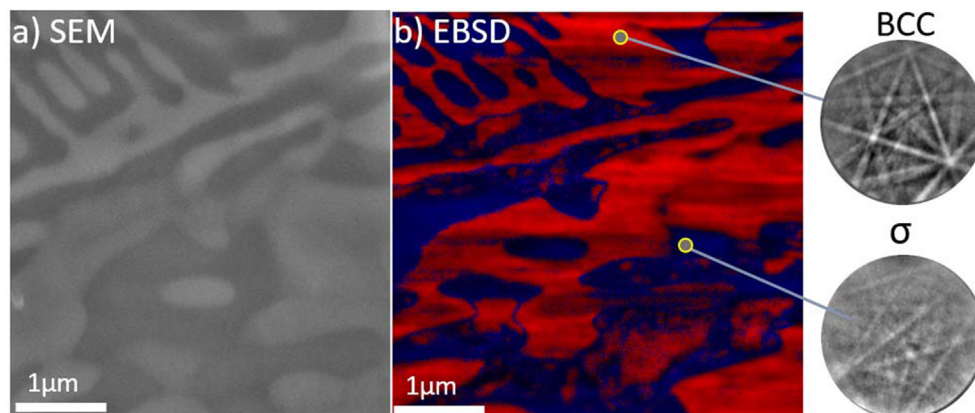


Fig. 4. (a) SEM and (b) EBSD images of the same area of the sample implanted with the D1 dose. Both the BCC and σ phases are clearly visible. The representative Kikuchi patterns are also shown.

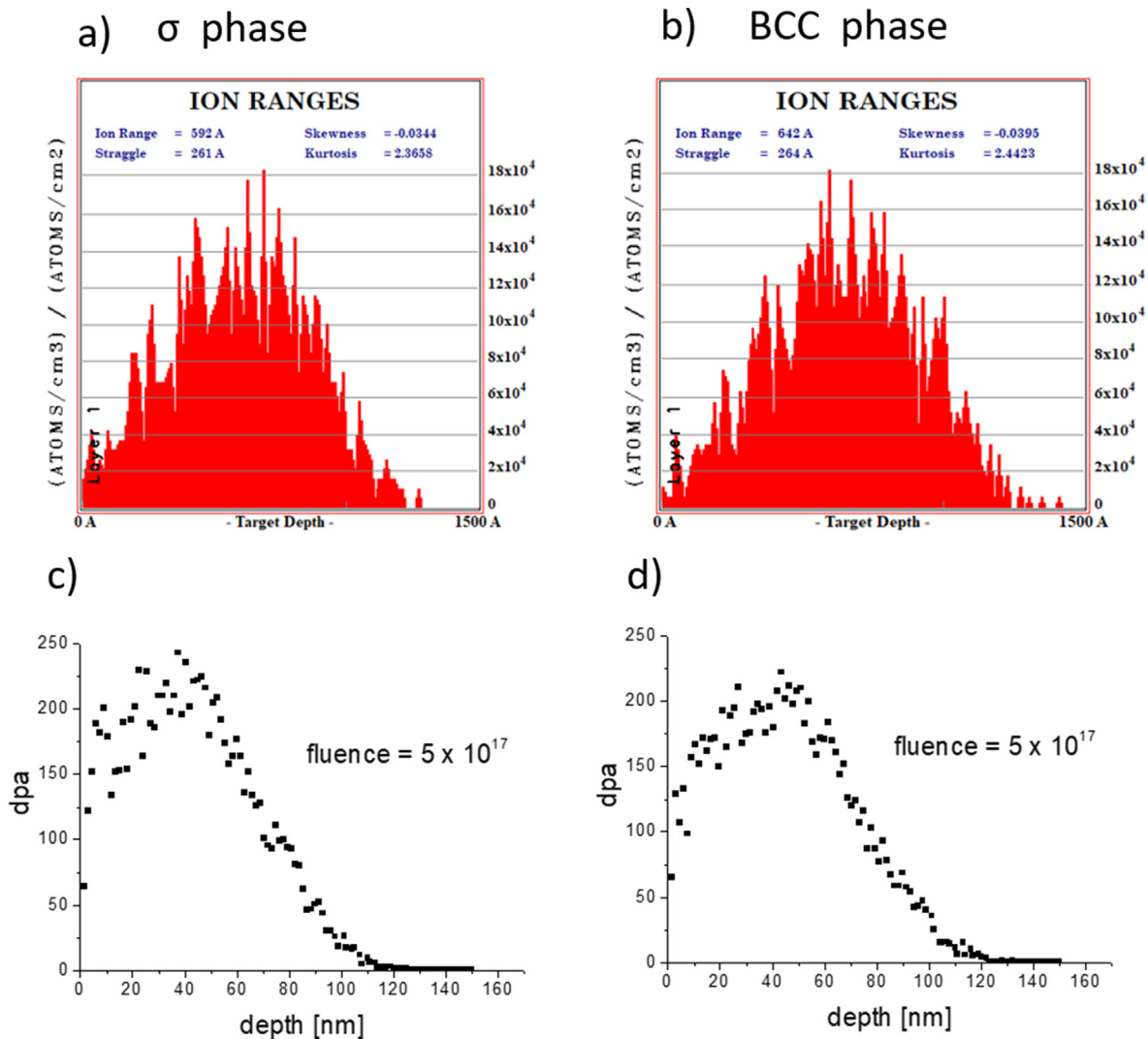


Fig. 5. (a and b) SRIM calculations and histograms of ion ranges during ion implantation for the σ and BCC phase, respectively. (c, d) dpa as a function of penetration depth for the σ and BCC phase, respectively.

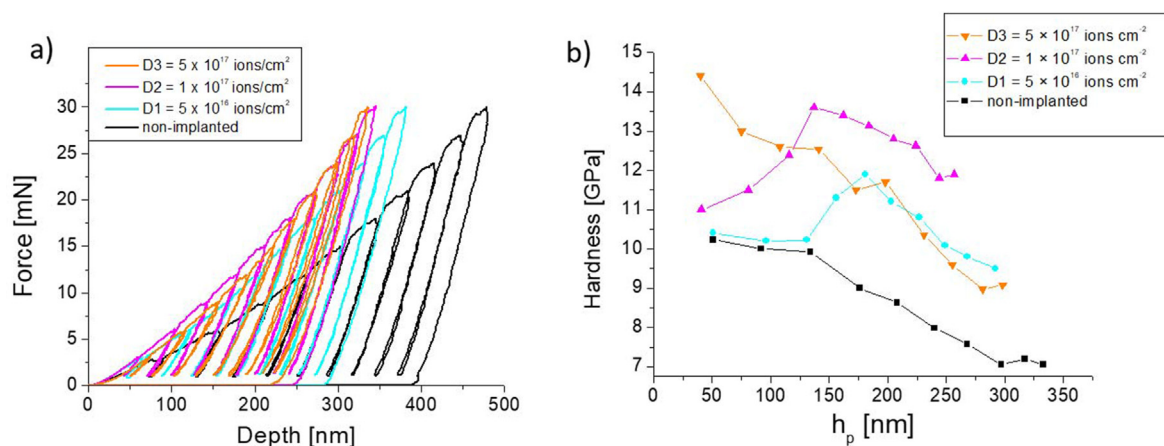


Fig. 6. (a) Multi-cycle indentation curves and (b) the corresponding hardness results from the Oliver–Pharr method. Lines connecting the measurement points are so called “guide-for-an-eye.”

The hardness increases as the indentation depth decreases, until it reaches its maximum at 187 and 137 nm for the D1 and D2 samples, respectively. The maximum is not visible in the case of the

D3 sample. For the highest applied fluence, the hardness increases as the indentation depth decreases, similarly to the bulk specimen, but with significantly higher hardness values. Of note, for lower

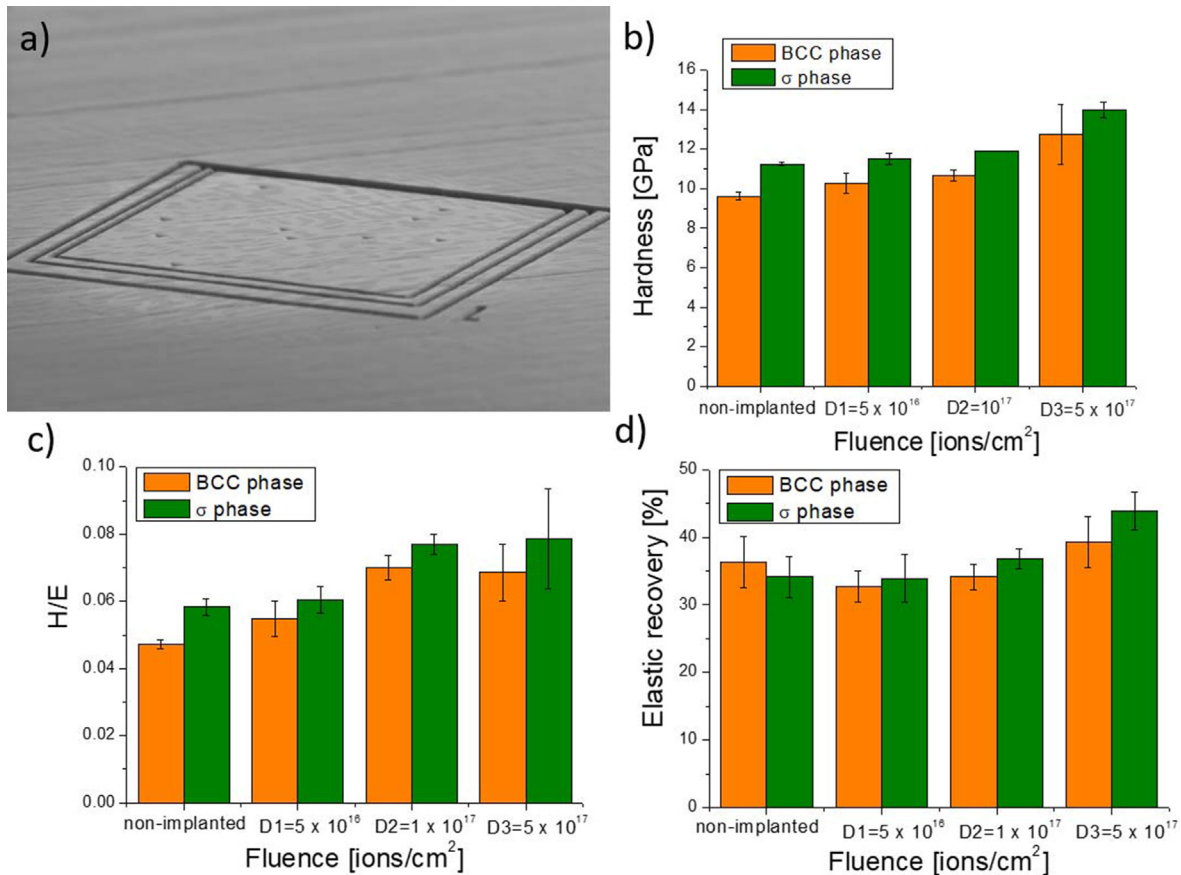


Fig. 7. (a) FIB-marked area where the indentation was performed with the maximum load (3 mN), with visible residual imprints. The graphs show the results of (b) hardness, (c) the hardness to Young's modulus (H/E) ratio, and (d) elastic recovery obtained from indentation curves and the Oliver–Pharr method.

indentation depths, the D3 sample shows the greatest hardness, whereas for indentation depths deeper than about 130 nm, the D2 sample exhibits the greatest hardness.

It should be noted that for the larger loads, the areas of the imprints and indentation depths were too large to study the differences between both phases of this eutectic alloy. Hence, an *in situ* SEM nanoindentation device with an extremely precise and accurate positioning system was applied to perform small imprints (3 mN maximal load) in both phases. The results are shown in Fig. 7. Fig. 7a shows the area (marked with a

focused-ion beam [FIB]) in which the imprints were made. A marking made with a FIB was applied to find the imprints more easily, and to choose those that were made exactly in the middle of the investigated phase. Fig. 7b presents the results of hardness determination. For each sample, the σ phase is harder than the BCC phase, and for both phases hardness increases with the ion fluence. Fig. 7c and d present the hardness to Young's modulus (H/E) ratio and elastic recovery (W_e), respectively. Both parameters can be used to determine a material's resistance to cracking [18].

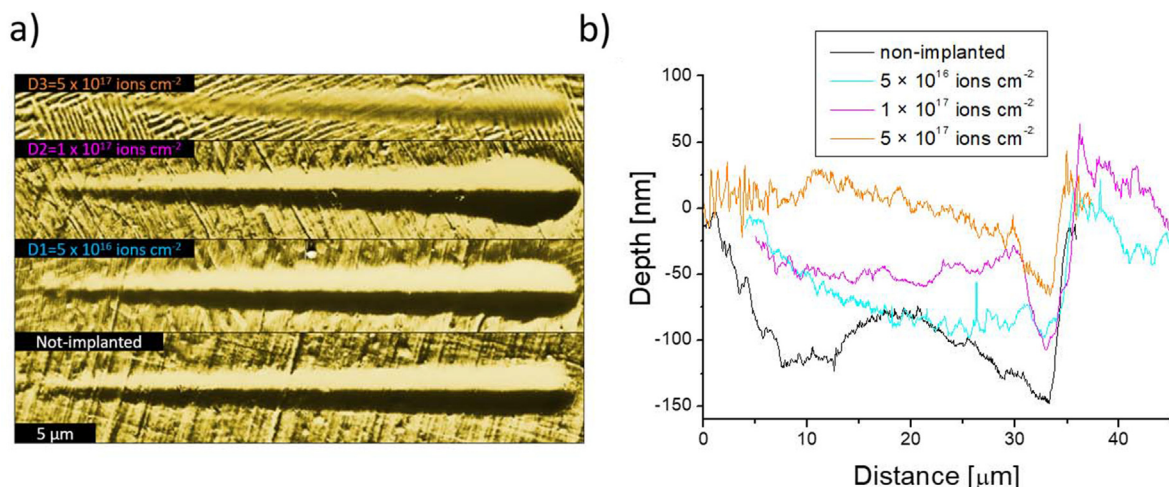


Fig. 8. The results of the scratch tests: (a) topography of wear track after the scratch tests and (b) the profiles of the representative wear tracks.

Finally, Fig. 8 shows the results of the scratch tests. Fig. 8a presents an example of two scratches performed on the D2 sample and measured by using AFM. Fig. 8b is a plot of the longitudinal profiles obtained for each sample. The sample irradiated with the highest ion fluence has the shallowest scratch; hence, its wear resistance is the highest. The bulk (non-implanted) specimen has the deepest scratch, and the wear resistance increases as the ion fluence increases.

4. Discussion

During ion implantation, elastic interactions between N^+ ions and atoms in the AlCoCrFeNiTi_{0.2} alloy result in numerous atomic displacements. If the energy transferred from the N^+ ion to an atom in the alloy is greater than the energy required to displace an atom from its lattice site, then the atom will be displaced from its position and travel through the lattice. If the displaced atom has enough energy, it continues displacing other atoms. This process is called a collision cascade. The final excess kinetic energy of the atom, which is not enough for another displacement, is transformed into the lattice vibrations. These lattice vibrations result in a localized increase in temperature, up to several thousand kelvins, which lasts a few picoseconds and is known as a thermal spike [24]. Hence, the phase transformation observed in the studied alloy could be caused by two different effects—radiation-enhanced diffusion and the thermal spikes—and/or by their combination.

In the present work, we have observed that the BCC phase is stable under ion irradiation. This finding is consistent with many other papers that have reported enhanced primary defect resistance of metals with the BCC structure [25]. On the other hand, it has been reported that the σ phase can transform into the BCC phase due to interaction with high-energy particles. For example, Anada et al. [26] have shown that σ -CrFe can transform under electron radiation into the BCC phase. We have reported a similar effect in this work for the σ phase present in the AlCoCrFeNiTi_{0.2} alloy subjected to ion irradiation. Thermal spikes may be responsible for this phase transformation, especially due to the fact that HEAs are known for their reduced thermal conductivity in cascade dynamics. Instead of being dissipated over a wide volume, the final excess kinetic energy is more localized and concentrated, a phenomenon that could increase phonon scattering. This should give more energy and time for atom reorganization and phase transformation. It should be noted that the precise conditions for the phase transformation are unknown, mainly due to the fact that our fundamental understanding of intermetallic phases in HEAs is still

very limited. Although it is generally agreed that HEAs and CCAs usually consist of simple solid solution phases with the face-centered cubic (FCC) or BCC structure, there have been reports of intermetallic phases in these materials [2]. To date, there are two stability criteria for σ phase formation in CCAs: one based on the valence electron concentration (VEC) and the second based on the alloy composition [27,28]. Unfortunately, these criteria are insufficient to explain the effects observed here. Furthermore, it is worth noting that the σ phase usually increases in alloys over time and during annealing [29,30]. In this work, we have observed an opposite effect due to ion implantation.

Fig. 9 presents SEM images of sample cross-sections. Not surprisingly, the D3 sample shows the most significant changes in the surface structure (Fig. 9d). Of note, although both phases are strongly affected by the interaction with the ions, there are no voids. Hence, the investigated alloy is resistant to void swelling even when dpa is > 200 . However, one question remains: What has happened with the nitrogen? It should somehow be embedded in the crystal structure of the material.

According to Li and Zhang [31], a solid solution phase in multi-component alloys with high-entropy mixing could be formed and is stable if the maximum misfit between the solute atoms is $< 12\%$ and the mixing enthalpy of the alloy (ΔH_{mix}) is from -40 to 10 kJ/mol. The difference in the atomic radius ΔR_i can be calculated for the i -th element using the following equations:

$$\Delta R_i = |R_a - R_i|/R_a$$

$$R_a = \sum_{i=1}^n R_i C_i, \quad (6)$$

where R_a is the average atomic radius, R_i is atomic radius of component, and C_i is the molar percentage of the component. If one takes C_i as %at obtained from EDS (shown in Table 1) and R_i from the reference [32], then for both the BCC and σ phases, $\Delta R_{i \max}$ is obtained for titanium and is equal to 13% and 16.5% , respectively. In view of the first criterion mentioned above, both phases are unstable but the σ phase is less stable than BCC.

Furthermore, ΔH_{mix} could be determined as follows:

$$\Delta H_{mix} = \sum_{i=1, i \neq j}^n \Omega_{ij} C_i C_j, \quad (7)$$

where Ω_{ij} is the regular melt interaction parameter between the i -th and j -th elements, and c_i is the atomic percentage of the i -th component. According to Takeuchi and Inoue [33], Ω_{ij} can be represented by the following expression:

$$\Omega_{ij} = 4H_{AB}^{mix}, \quad (8)$$

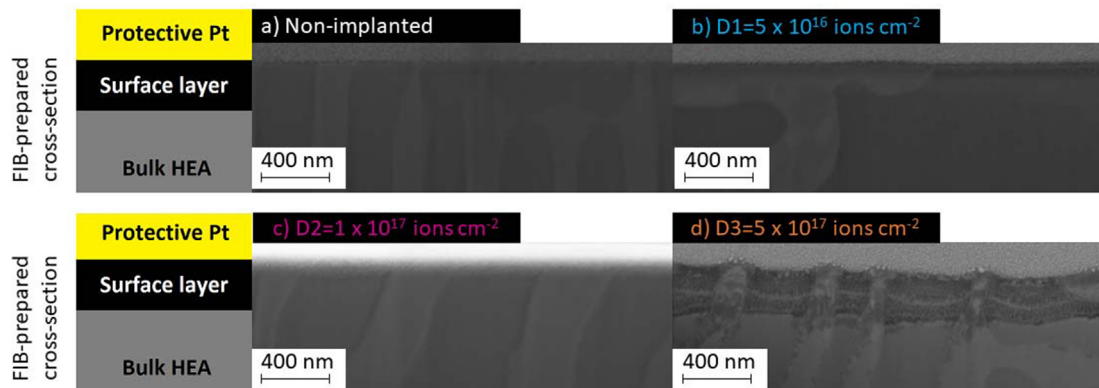


Fig. 9. Cross-sections through the sample surfaces. There are significant changes in the sample structure only for the D3 sample (exposed to the highest fluence). It should be noted that the protective platinum (Pt) layer has been deposited before FIB cutting to avoid implanting gallium (Ga) ions on the surface.

Table 2Results of calculation of $\Delta R_{i \max}$ and ΔH_{mix} for the σ and BCC phases.

	Bulk (non-implanted)		D1		D2		D3	
	BCC	σ	BCC	Σ	BCC	σ	BCC	σ
$\Delta R_{i \max}$	13%	16.5%	15%	18.6%	15%	18%	41%	45%
ΔH_{mix} [kJ/mol]	−16.71	−6.79	−26.43	−17.33	−25.82	−16.68	−87.2	−84.52

where H_{AB}^{mix} is the mixing enthalpy of a binary liquid alloy, which can be obtained from Takeuchi and Inoue [32]. ΔH_{mix} is −16.71 kJ/mol for the BCC phase and −6.79 kJ/mol for the σ phase it is. Hence, both phases fulfill the second criterion.

The situation changes drastically if the nitrogen ions are introduced into the equations. One can take the nitrogen ion concentration obtained from EDS (Fig. 1) and then determine $\Delta R_{i \max}$ and ΔH_{mix} for both phases. The calculated results (Table 2) indicate that if the above-mentioned criteria can be used for ion-implanted material, then the solid solutions cannot be created, especially in the case of the D3 sample, where both $\Delta R_{i \max}$ and ΔH_{mix} are out of the allowed range. The obtained structures should be highly unstable. On the other hand, the investigated samples have both the BCC and σ phases with a high nitrogen ion concentration, and XRD detected only small amounts of simple nitrides. Furthermore, SEM images of the cross-section indicate significant changes in the sample structures (Fig. 9). Our preliminary hypothesis is that although the above-discussed criteria are not fulfilled, the nitrogen ion implantation has led to the creation of new high-entropy ceramic material. This hypothesis is partially confirmed by the XRD results due to the fact that the observed peaks do not fit any known nitrides from either ICDD-4 + or COD. Furthermore, the presented results of this study are totally different from the results obtained for plasma nitriding of HEAs, where XRD clearly indicated the presence of simple nitrides [34,35], or only peak broadening was observed [36]. It is only clear that the mechanism of nitrogen incorporation into the HEA structure is significantly different for ion implantation, where the ions have energy equal to 50 keV, than for plasma nitriding where the plasma is accelerated by a voltage usually < 1 keV and thermal treatment plays a more significant role. Of note, AlCoCrFeNiTi_{0.2} consists of elements that are strong nitride formers (Ti and Al) and weak nitride formers (Co, Cr, and Fe) [37]. Furthermore, Al forms a covalent nitride, which is stable in the form of a hexagonal wurtzite, in contrast to all the other elements in the studied alloy, which form nitrides with the NaCl-type structure. Taking the above into account and the fact that high-dose nitrogen ion implantation could easily create new, metastable compounds [38], the exact structure of the created material is not obvious and requires additional investigation.

The second effect observed in this work is the hardening of both the BCC and σ phases. Although a number of investigations have reported rather low irradiation hardening of BCC HEAs [39–41], there are a few papers that have reported the opposite for specific HEAs, namely significant hardening in CrFeNi-based alloys [42,43]. Cr, Fe, and Ni are present in the alloy studied in this investigation, which may explain the approximately 25% increase in hardness after ion implantation. Furthermore, EDS spectra (Fig. 2a) indicate a uniform distribution of nitrogen in the implanted surface, and nitrogen can form hard nitrides. However, as mentioned previously, almost no simple nitrides have been detected by XRD. Hence, we have tentatively attributed the significant increase in hardness to the creation of high-entropy nitride. On the other hand, the most surprising result in our study is the fact that in addition to the increased hardness, the H/E ratio and the elastic recovery are also higher. The increase in these parameters suggests greater resistance to cracking and higher ductility, which may also indicate good tolerance to irradiation damage. Furthermore, simi-

lar effects—hardening and an increase in the H/E ratio and elastic recovery—have been observed for the σ phase. Due to the fact that there are only a few papers about σ phase irradiation, and in almost all the cases not in HEAs, we claim that we are the first to observe these effects. These findings are promising and should be explored further.

One should note that the hardness does not simply increase as the indentation depth decreases. In Fig. 6b, there are clearly visible hardness peaks for the D1 and D2 samples. There are factors that interplay, including: (1) work hardening of the surface layer due to polishing, (2) change in the crystal structure due to implantation, and (3) change in the chemical composition (nitrogen atoms added). These effects can be separated due to the fact that nanoindentation was performed on the bulk, non-implanted specimen, and then the results were compared for each phase. Decreasing hardness with indentation depth for non-implanted sample may be caused by the decreasing influence of the hardened surface layer. However, the D3 sample, with the highest ion dose, has the same hardness trend but exhibits higher values, while it is expected that ion bombardment catastrophically changes the structure in the range of a few hundreds of nanometers (thus damaging the hardened structure of the surface layer). The decreased hardness with indentation depth is rather a result of the indentation size effect of the Berkovich tip. Taken together, neither the hardening nor the size effect is a cause of the peaks for the D1 and D2 samples. Hence, the origin of the peaks is not clear. We have tentatively attributed it to the changes in the nitrogen atom distribution depending on the ion dose, which are not taken into account by relatively simple SRIM calculations, and the increase in hardness with nitrogen concentration. This would explain the peaks for the D1 and D2 samples. The left shift of the peak for the D2 sample compared with the D1 sample suggests that the material is saturated with nitrogen atoms at a shallower depth. The lack of the peak for the D3 sample, therefore, means that the structure in terms of the nitrogen concentration is more or less homogeneously saturated, so only the above-mentioned indentation size effect is visible for the D3 sample. However, it should be confirmed by Secondary ion mass spectrometry (SIMS) measurements, which we plan to perform in our subsequent studies concerning ion beam interactions with high-entropy materials.

Finally, we have also observed a significant increase in wear resistance (Fig. 8). It is generally accepted that hardness as well as H/E ratio play a substantial role in wear resistance [44]. In Fig. 6b and c, it can be seen that both of these parameters for both phases increase due to implantation. However, a closer examination of these graphs shows that for hardness there is a more pronounced increase only for the D3 sample, while for the H/E ratio the increase occurs for both the D2 and D3 samples. The scratch tests provide additional information that greater hardness for the D3 sample is more important than a higher H/E ratio in terms of wear resistance, which can be concluded based on the size of tracks as well as their depth profile.

5. Conclusion

We have shown that ion implantation of the AlCoCrFeNiTi_{0.2} HEA has led to unexpected XRD spectrum, phase transformation,

and hardening of the surface layer. In contrast to thermal processes such as nitriding, nitrogen ion implantation does not lead to the creation of simple nitrides; rather, there are unidentified peaks. These peaks correspond to the BCC and σ phases, similarly to the bulk (virgin) specimen, but their ratio changes for the ion-implanted samples. In general, we have confirmed the BCC phase stability and have observed the σ to BCC phase transformation. We have also found hardening of the BCC and σ phases. Simultaneously, there is a surprising increase in the H/E ratio and elastic recovery of both phases. Although the proposed criteria of possible composition of high-entropy materials have not been fulfilled, we tentatively attribute our results to the creation of new high- or medium-entropy ceramics in the implanted samples. The new material also has promising and interesting properties, but the mechanism of its creation and its exact structure require additional, extensive research.

Data availability

The raw data and processed data required to reproduce these findings are available from the corresponding author upon request.

Declaration of Competing Interest

The authors declare that they have no known competing financial interests or personal relationships that could have appeared to influence the work reported in this paper.

Appendix A. Supplementary material

Supplementary data to this article can be found online at <https://doi.org/10.1016/j.matdes.2022.110568>.

References

- J.W. Yeh, S.K. Chen, S.J. Lin, J.Y. Gan, T.S. Chin, T.T. Shun, C.H. Tsau, S.Y. Chang, Nanostructured high-entropy alloys with multiple principal elements: Novel alloy design concepts and outcomes, *Adv. Eng. Mater.* 6 (2004) 299–303, <https://doi.org/10.1002/adem.200300567>.
- M.-H. Tsai, J.-W. Yeh, High-entropy alloys: a critical review, *Mater. Res. Lett.* 2 (3) (2014) 107–123, <https://doi.org/10.1080/21663831.2014.912690>.
- A.M. Manzoni, U. Glatzel, New multiphase compositionally complex alloys driven by the high entropy alloy approach, *Mater. Charact.* 147 (2019) 512–532, <https://doi.org/10.1016/j.matchar.2018.06.036>.
- A. Shabani, M.R. Toroghinejad, Investigation of microstructure, texture, and mechanical properties of FeCrCuMnNi multiphase high entropy alloy during recrystallization, *Mater. Charact.* 154 (2019) 253–263, <https://doi.org/10.1016/j.matchar.2019.05.043>.
- S. Alvi, D.M. Jarzabek, M.G. Kohan, D. Hedman, P. Jenczyk, M.M. Natile, A. Vomiero, F. Akhtar, Synthesis and mechanical characterization of a CuMoTaWV high-entropy film by magnetron sputtering, *ACS Appl. Mater. Interfaces* 12 (18) (2020) 21070–21079, <https://doi.org/10.1021/acsami.0c02156>.
- E.J. Pickering, A.W. Carruthers, P.J. Barron, S.C. Middleburgh, D.E.J. Armstrong, A.S. Gandy, High-entropy alloys for advanced nuclear applications, *Entropy* 23 (2021) 1–28, <https://doi.org/10.3390/e23010098>.
- X. Wang, H. Yao, Z. Zhang, X. Li, C. Chen, L. Yin, K. Hu, Y. Yan, Z. Li, B. Yu, F. Cao, X. Liu, X. Lin, Q. Zhang, Enhanced thermoelectric performance in high entropy alloys Sn_{0.25}Pb_{0.25}Mn_{0.25}Ge_{0.25}Te, *ACS Appl. Mater. Interfaces* 13 (16) (2021) 18638–18647, <https://doi.org/10.1021/acsami.1c00221>.
- J. Startt, A. Kustas, J. Pegues, P. Yang, R. Dingreville, Compositional effects on the mechanical and thermal properties of MoNbTaTi refractory complex concentrated alloys, *Mater. Des.* 213 (2022), <https://doi.org/10.1016/j.matdes.2021.110311>.
- W.O. Herrera Martínez, P. Giudici, N.B. Correa Guerrero, M.L. Ibarra, M.D. Perez, Effect of high energy proton irradiation on MAPb(3) films for space applications observed by micro-Raman spectroscopy, *Mater. Adv.* 1 (6) (2020) 2068–2073.
- A.D. Pogrebnjak, O.V. Bondar, S.O. Borba, K. Piotrowska, O. Boiko, Structure and physicochemical properties of nanostructured (TiHfZrNbV)N coatings after implantation of high fluences of N⁺ (10¹⁸ cm⁻²), *Acta Phys. Pol. A* 132 (2) (2017) 217–221.
- X. Xiao, L. Yu, Nano-indentation of ion-irradiated nuclear structural materials: a review, *Nucl. Mater. Energy* 22 (2020) 100721, <https://doi.org/10.1016/j.nme.2019.100721>.
- F.A. Garner, M.B. Toloczko, B.H. Sencer, Comparison of swelling and irradiation creep behavior of fcc-austenitic and bcc-ferritic/martensitic alloys at high neutron exposure, *J. Nucl. Mater.* 276 (1–3) (2000) 123–142, [https://doi.org/10.1016/S0022-3115\(99\)00225-1](https://doi.org/10.1016/S0022-3115(99)00225-1).
- M.L. Jenkins, M.A. Kirk, W.J. Phythian, Experimental studies of cascade phenomena in metals, *J. Nucl. Mater.* 205 (1993) 16–30, [https://doi.org/10.1016/0022-3115\(93\)90067-9](https://doi.org/10.1016/0022-3115(93)90067-9).
- K. Vortler, N. Juslin, G. Bonny, L. Malerba, K. Nordlund, The effect of prolonged irradiation on defect production and ordering in Fe-Cr and Fe-Ni alloys, *J. Phys. Condens. Matter* 23 (2011), <https://doi.org/10.1088/0953-8984/23/35/355007>.
- P.J. Doyle, K.M. Benensky, S.J. Zinkle, Modeling the impact of radiation-enhanced diffusion on implanted ion profiles, *J. Nucl. Mater.* 509 (2018) 168–180, <https://doi.org/10.1016/j.jnucmat.2018.06.042>.
- M. Nastasi, J.W. Mayer, Thermodynamics and kinetics of phase-transformations induced by ion irradiation, *Mater. Sci. Rep.* 6 (1) (1991) 1–51, [https://doi.org/10.1016/0920-2307\(91\)90003-6](https://doi.org/10.1016/0920-2307(91)90003-6).
- A.S. Gandy, B. Jim, G. Coe, D. Patel, L. Hardwick, S. Akhmadaliev, N. Reeves-McLaren, R. Goodall, High temperature and ion implantation-induced phase transformations in novel reduced activation Si-Fe-V-Cr (-Mo) high entropy alloys, *Front. Mater.* 6 (2019) 146, <https://doi.org/10.3389/fmats.2019.00146>.
- J. Musil, Flexible hard nanocomposite coatings, *RSC Adv.* 5 (74) (2015) 60482–60495, <https://doi.org/10.1039/C5RA09586G>.
- M. Yuan, X. Zhang, A.M.A. Saeedi, W. Cheng, C. Guo, B. Liao, X. Zhang, M. Ying, G.A. Gehring, Study of the radiation damage caused by ion implantation in ZnO and its relation to magnetism, *Nucl. Instrum. Methods Phys. Res. B Beam Interact. Mater. At.* 455 (2019) 7–12, <https://doi.org/10.1016/j.nimb.2019.06.013>.
- L.B. McCusker, R.B. Von Dreele, D.E. Cox, D. Louër, P. Scardi, Rietveld refinement guidelines, *J. Appl. Crystallogr.* 32 (1) (1999) 36–50, <https://doi.org/10.1107/S0021889898009856>.
- B.D. Cullity, Elements of X-ray Diffraction, Addison-Wesley, Boston, MA, 1978.
- P.F. Fewster, N.L. Andrew, V. Holy, K. Barmak, X-ray diffraction from polycrystalline multilayers in grazing-incidence geometry: measurement of crystallite size depth distribution, *Phys. Rev. B* 72 (2005), <https://doi.org/10.1103/PhysRevB.72.174105>.
- S.J. Skrzypek, M. Goly, W. Ratuszek, M. Kowalski, Non-destructive quantitative phase and residual stress analysis versus depth using grazing X-ray diffraction, *Solid State Phenom.* 130 (2007) 47–52, <https://doi.org/10.4028/www.scientific.net/SSP.130.47>.
- S. Skirlo, M.J. Demkowicz, The role of thermal spike compactness in radiation-induced disordering and Frenkel pair production in Ni₃Al, *Scr. Mater.* 67 (7–8) (2012) 724–727, <https://doi.org/10.1016/j.scriptamat.2012.06.029>.
- L. Wei, Y. Li, G. Zhao, Q. Zheng, J. Li, Z. Zeng, Key factors in radiation tolerance of BCC metals under steady state, *Nucl. Instrum. Methods Phys. Res. B Beam Interact. Mater. At.* 455 (2019) 134–139, <https://doi.org/10.1016/j.nimb.2019.06.032>.
- S. Anada, T. Nagase, K. Kobayashi, H. Yasuda, H. Mori, Phase stability of sigma-CrFe intermetallic compound under fast electron irradiation, *Acta Mater.* 71 (2014) 195–205, <https://doi.org/10.1016/j.actamat.2014.03.023>.
- M.-H. Tsai, K.-Y. Tsai, C.-W. Tsai, C. Lee, C.-C. Juan, J.-W. Yeh, Criterion for sigma phase formation in Cr- and V-containing high-entropy alloys, *Mater. Res. Lett.* 1 (4) (2013) 207–212, <https://doi.org/10.1080/21663831.2013.831382>.
- M.-H. Tsai, K.-C. Chang, J.-H. Li, R.-C. Tsai, A.-H. Cheng, A second criterion for sigma phase formation in high-entropy alloys, *Mater. Res. Lett.* 4 (2) (2016) 90–95, <https://doi.org/10.1080/21663831.2015.1121168>.
- B. Ren, Z.X. Liu, B. Cai, M.X. Wang, L. Shi, Aging behavior of a CuCr₂Fe₂NiMn high-entropy alloy, *Mater. Des.* 33 (2012) 121–126, <https://doi.org/10.1016/j.matdes.2011.07.005>.
- C.G. Schon, M.A. Tunes, R. Arroyave, J. Agren, On the complexity of solid-state diffusion in highly concentrated alloys and the sluggish diffusion core-effect, *Calphad* 68 (2020), <https://doi.org/10.1016/j.calphad.2019.101713>.
- A. Li, X. Zhang, Thermodynamic analysis of the simple microstructure of AlCrFeNiCu high-entropy alloy with multi-principal elements, *Acta Metall. Sin. Lett.* 22 (3) (2009) 219–224, [https://doi.org/10.1016/S1006-7191\(08\)60092-7](https://doi.org/10.1016/S1006-7191(08)60092-7).
- A. Takeuchi, A. Inoue, Classification of bulk metallic glasses by atomic size difference, heat of mixing and period of constituent elements and its application to characterization of the main alloying element, *Mater. Trans.* 46 (12) (2005) 2817–2829, <https://doi.org/10.2320/matertrans.46.2817>.
- A. Takeuchi, A. Inoue, Quantitative evaluation of critical cooling rate for metallic glasses, *Mater. Sci. Eng. A Struct. Mater. Prop. Microstruct. Process.* 304 (2001) 446–451, [https://doi.org/10.1016/S0921-5093\(00\)01446-5](https://doi.org/10.1016/S0921-5093(00)01446-5).
- W.-Y. Tang, J.-W. Yeh, Effect of aluminum content on plasma-nitrided Al (x) CoCrCuFeNi high-entropy alloys, *Metall. Mater. Trans. A* 40 (6) (2009) 1479–1486, <https://doi.org/10.1007/s11661-009-9821-5>.
- W.-Y. Tang, M.-H. Chuang, H.-Y. Chen, J.-W. Yeh, Microstructure and mechanical performance of new Al_{0.5}CrFe_{1.5}MnNi_{0.5} high-entropy alloys improved by plasma nitriding, *Surf. Coat. Technol.* 204 (20) (2010) 3118–3124, <https://doi.org/10.1016/j.surfcoat.2010.02.045>.
- R. Wang, Y. Tang, Z. Lei, Y. Ai, Z. Tong, S. Li, Y. Ye, S. Bai, Achieving high strength and ductility in nitrogen-doped refractory high-entropy alloys, *Mater. Des.* 213 (2022), <https://doi.org/10.1016/j.matdes.2021.110356>.
- E. Lewin, Multi-component and high-entropy nitride coatings-A promising field in need of a novel approach, *J. Appl. Phys.* 127 (2020), <https://doi.org/10.1063/1.5144154>.

- [38] C. Uslu, B. Park, D.B. Poker, Synthesis of metastable carbon-silicon-nitrogen compounds by ion implantation, *J. Electron. Mater.* 25 (1) (1996) 23–26, <https://doi.org/10.1007/BF02666169>.
- [39] A. Kareer, J.C. Waite, B. Li, A. Couet, D.E.J. Armstrong, A.J. Wilkinson, Short communication: 'Low activation, refractory, high entropy alloys for nuclear applications', *J. Nucl. Mater.* 526 (2019), <https://doi.org/10.1016/j.jnucmat.2019.151744> 151744.
- [40] O. El-Atwani, N. Li, M. Li, A. Devaraj, J.K.S. Baldwin, M.M. Schneider, D. Sobieraj, J.S. Wrobel, D. Nguyen-Manh, S.A. Maloy, E. Martinez, Outstanding radiation resistance of tungsten-based high-entropy alloys, *Sci. Adv.* 5 (2019) eaav2002, <https://doi.org/10.1126/sciadv.aav2002>.
- [41] M. Moschetti, A. Xu, B. Schuh, A. Hohenwarter, J.-P. Couzinié, J.J. Kruzic, D. Bhattacharyya, B. Gludovatz, On the room-temperature mechanical properties of an ion-irradiated TiZrNbHfTa refractory high entropy alloy, *JOM* 72 (1) (2020) 130–138, <https://doi.org/10.1007/s11837-019-03861-6>.
- [42] N.A.P.K. Kumar, C. Li, K.J. Leonard, H. Bei, S.J. Zinkle, Microstructural stability and mechanical behavior of FeNiMnCr high entropy alloy under ion irradiation, *Acta Mater.* 113 (2016) 230–244, <https://doi.org/10.1016/j.actamat.2016.05.007>.
- [43] L. Yang, H. Ge, J. Zhang, T. Xiong, Q. Jin, Y. Zhou, X. Shao, B.o. Zhang, Z. Zhu, S. Zheng, X. Ma, High He-ion irradiation resistance of CrMnFeCoNi high-entropy alloy revealed by comparison study with Ni and 304SS, *J. Mater. Sci. Technol.* 35 (3) (2019) 300–305, <https://doi.org/10.1016/j.jmst.2018.09.050>.
- [44] A. Leyland, A. Matthews, On the significance of the H/E ratio in wear control: a nanocomposite coating approach to optimised tribological behaviour, *Wear* 246 (2000) 1–11, [https://doi.org/10.1016/S0043-1648\(00\)00488-9](https://doi.org/10.1016/S0043-1648(00)00488-9).